Am J Nucl Med Mol Imaging 2026;16(5):232-241
www.ajnmmi.us /ISSN:2160-8407/ajnmmi0175954

Original Article

Radiosynthesis and evaluation of an imidazo[4,5-*b*]pyridin-2-one-derived radioligand for imaging GluN2B-containing NMDA receptors

Yinlong Li[1*], Zhendong Song[1*], Taoqian Zhao[1], Haofeng Shi[1], Yanwei Jiang[1], Yuanfang Jiang[1], Jiahui Chen[1], Xin Zhou[1], Lingxin Meng[1], Ruihu Song[1], Zhenkun Sun[2], Siyan Feng[1], Hongjie Yuan[2], Achi Haider[1], Steven H. Liang[1,3]

[1]Department of Radiology and Imaging Sciences, Emory University, 1364 Clifton Road, Atlanta, Georgia 30322, The United States; [2]Department of Pharmacology and Chemical Biology, Emory University School of Medicine, Atlanta, Georgia 30322, The United States; [3]Wallace H. Coulter Department of Biomedical Engineering, Georgia Institute of Technology and Emory University, Atlanta, Georgia 30332, The United States. [*]Equal contributors.

Received August 11, 2026; Accepted September 3, 2026; Epub October 25, 2026; Published October 30, 2026

Abstract: GluN2B-containing *N*-methyl-D-aspartate receptors (NMDARs) are key mediators of synaptic plasticity in the brain and have been implicated in Alzheimer's and Parkinson's disease. However, no radiofluorinated positron emission tomography (PET) radioligand is available for mapping GluN2B in the living human brain. Herein, we report the radiosynthesis and preclinical evaluation of [^{18}F]N2B-2502, an ^{18}F-labeled imidazo[4,5-*b*]pyridin-2-one derivative designed to target GluN2B-containing NMDARs. Nucleophilic radiofluorination of the corresponding precursor afforded [^{18}F]N2B-2502 in excellent radiochemical purity (>98%) and molar activity (>37 GBq/μmol). *In vitro* autoradiography in rat brain sections revealed high uptake in the hippocampus, thalamus, striatum, and cortex, consistent with the known regional distribution of GluN2B subunit expression. However, PET imaging in CD-1 mice revealed low brain uptake that increased following P-glycoprotein (P-gp) inhibition, indicating that [^{18}F]N2B-2502 might be a P-gp substrate. Further structure-activity relationship optimization based on this scaffold is warranted to achieve high brain penetration for *in vivo* GluN2B-NMDAR imaging.

Keywords: GluN2B, NMDARs, fluorine-18, positron emission tomography, imidazo[4,5-*b*]pyridin-2-one

Introduction

N-methyl-D-aspartate receptors (NMDARs) are heterotetrameric ligand-gated ion channels assembled from two obligatory GluN1 subunits and two GluN2 or GluN3 subunits [1, 2]. Those channels carry the slow, Ca^{2+}-permeable component of excitatory transmission and mediate synaptic plasticity [3]. GluN2B (NR2B, encoded by *GRIN2B*) is the dominant GluN2 isoform in the immature forebrain [3, 4]. In the adult brain, GluN2B is abundant in the hippocampus, striatum, thalamus and cortex, and expressed at low levels in the cerebellum [5]. *GRIN2B* loss- and gain-of-function variants result in a spectrum of developmental and epileptic encephalopathies [6], and GluN2B-mediated excitotoxicity has been implicated in Alzheimer's disease (AD) [7] and Parkinson's disease (PD) [8]. Subunit-selective negative allosteric modulators (NAMs) act at the GluN1/GluN2B amino-terminal domain interface. Based on this principle, ifenprodil, CP-101,606 (traxoprodil) and radiprodil have been developed to retain the efficacy of channel-blocking pan-NMDAR antagonists, while avoiding their psychotomimetic side effects [9]. However, while some of those modulators have entered clinical trials, no candidate has been advanced to larger phase III trials yet. Quantifying GluN2B in the living brain would support target engagement studies and regional receptor measurements in patients, thereby facilitating drug development efforts.

Positron emission tomography (PET) is the established technique for measuring receptor availability in the living brain, and GluN2B radioligand development has been pursued for more than two decades (**Figure 1A**) [10, 11]. For example, (±)-[^{11}C]*threo*-1, a carbon-11 methoxy analogue of CP-101,606, was the first "prodil"-derived PET ligand for GluN2B. It bound the subunit specifically in rodent brain *in vitro*, but not *in vivo* [12]. An arylpyridinylmethylamine-derived ligand [^{11}C]HACH242 showed suitable brain kinetics in rhesus monkeys but low plasma stability and no specific binding [13]. Similarly, a 3-benzazepin-1-ol analog (*R*)-[^{11}C]Me-NB1 showed enantiomer-dependent selectivity and adequate brain uptake with reversible kinetics [14] and has been studied in humans [15]. Its binding in rat brains was abolished by (+)-pentazocine - raising potential concerns about σ1 receptor involvement in the PET signal in the brain [16]. Radiofluorinated analogs (*R/S*)-[^{18}F]OF-Me-NB1 and the related benzazepinol [^{11}C]NR2B-SMe were subsequently evaluated *in vivo*, however, no radiofluorinated candidate has been advanced to humans [17-22]. A 1,2,3,4-tetrahydroisoquinolin-7-ol-derived ligand [^{11}C]Ro04-5595 was reported to have limited brain uptake [23]. On the other hand, the pyrrolo[3,2-b]pyridinylacetamide NAMs [^{11}C]N2B-1810 and [^{11}C]N2B-1903 were displaceable in rat brain *in vitro* but gave low and uniform uptake in the living rat brain [24]. Although several of these ligands were selective for GluN2B *in vitro*, they showed low brain uptake or rapid metabolism *in vivo*.

https://doi.org/10.62347/AEBG3929

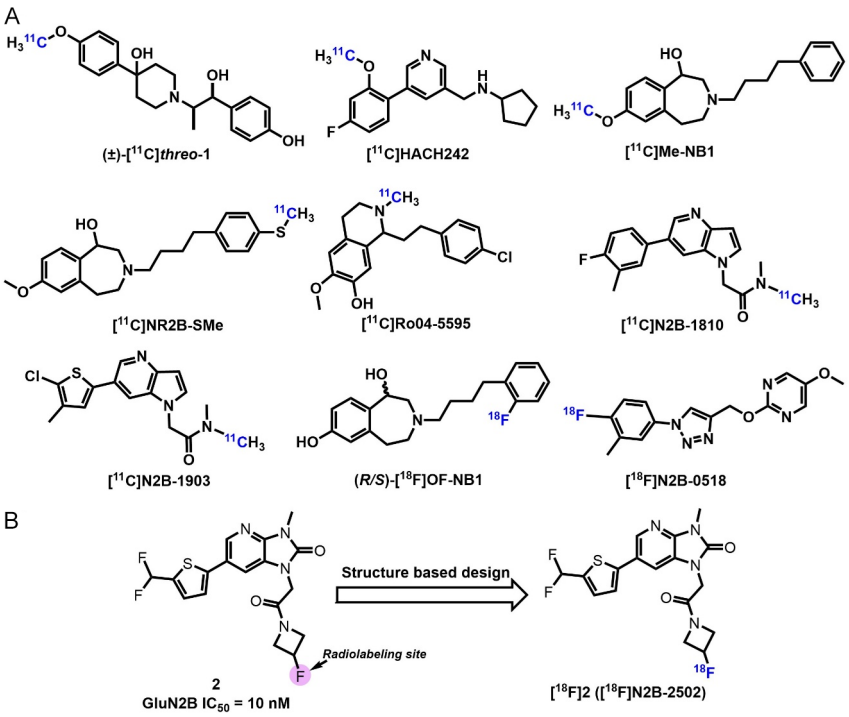


Figure 1. A. Representative PET ligands targeting GluN2B-containing NMDA receptors; B. Structures of compound 2 and the radioligand [^{18}F]2 ([^{18}F]N2B-2502).

The triazole-cored antagonist [^{18}F]N2B-0518 demonstrated *in vitro* specific binding in brain sections of rat and non-human primate (NHP), but has not been evaluated *in vivo* [25]. The availability of a radiofluorinated GluN2B-selective PET radioligand would expand the neuroscience toolbox by enabling satellite distribution to nuclear medicine facilities lacking an on-site cyclotron. Here we report the radiosynthesis of the imidazo[4,5-*b*]pyridin-2-one ligand [^{18}F]N2B-2502 and its evaluation in rodents (**Figure 1B**).

Results

Chemistry

The synthesis of compound 2 is outlined in **Scheme 1** [26]. Nitro compound 3 underwent nucleophilic aromatic substitution with methylamine in water to afford compound 4 in 99% yield. Reduction of the nitro group with iron and ammonium chloride gave amine 5 in 65% yield. Amine 5 was cyclized with carbonyldiimidazole (CDI) in THF to construct the imidazopyridinone core and deliver 6 in 79% yield. Alkylation of 6 with ethyl bromoacetate (7) under potassium carbonate in acetonitrile furnished ester 8 in 85% yield. Miyaura borylation of 8 with bis(pinacolato) diboron and potassium acetate under Pd(dppf)Cl_2 catalysis provided boronate 9 in 84% yield. Suzuki coupling of 9 with bromide 10 under Xphos-Pd-G2 catalysis produced compound 11 in 43% yield. Hydrolysis of the ethyl ester in 11 with lithium hydroxide gave acid 12. Amide coupling of 12 with 3-fluoroazetidine (13) using HATU and DIEA delivered the target compound 2 in 26% yield over two steps.

Pharmacology

The physicochemical and pharmacological properties of compound 2 are listed in **Table 1**. Compound 2 has a molecular weight of 396.39 and a logP of 1.64, and both values meet accepted criteria for PET ligands. The calculated logD is 1.60 (ACD Labs), and the experimental logD by the "shake-flask" method is 1.73, in agreement with the calculated value. The topological polar surface area (tPSA) is 84.99 Å^2, below the 90 Å^2 threshold for CNS penetration, and the CNS MPO score is 5.7. Compound 2 exhibited an IC_{50} of 10 nM against GluN2B, supporting further selectivity profiling [26].

Compound 2 was also evaluated against a panel of major CNS targets by the National Institute of Mental Health Psychoactive Drug Screening Program (PDSP) at a test concentration of 10 μM (**Figure 2**). Compound 2 exhibited no significant inhibition at most targets in the panel. Inhibition of peripheral benzodiazepine receptor (PBR) exceeded the 50% cutoff, and a secondary assay determined a K_i of 1.6 μM. Inhibition of sigma 2 reached 45.6%, below the 50% cutoff. Importantly, compound 2 showed no significant activity at sigma 1 (σ1), in contrast to the σ1-confounded binding reported for the benzazepinol-based GluN2B ligands.

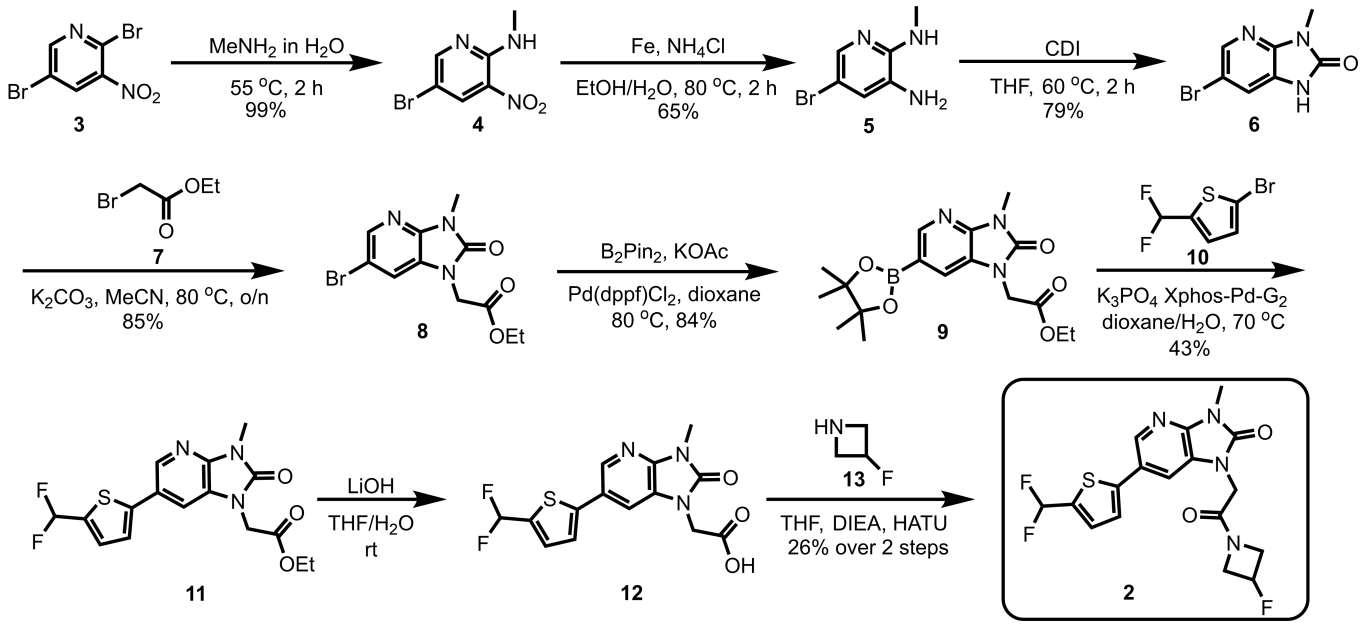
Radiochemistry

The synthesis of the tosylate precursor 17 is outlined in **Scheme 2**. Amide coupling of acid 14 with 3-hydroxyazetidine (15) under HATU and DIEA in THF afforded alcohol 16, and tosylation of the free hydroxyl group in 16 with TsCl, TEA, and DMAP in DCM delivered precursor 17 in 30% yield over the two steps.

With the precursor in hand, we moved forward to the radiosynthesis of [^{18}F]2, as illustrated in **Scheme 3**. Treatment of precursor 17 with [^{18}F]fluoride and tetraethylammonium bicarbonate (TEAB) in t-BuOH/MeCN (5:1, v/v) at 130°C for 5 min afforded [^{18}F]2 ([^{18}F]N2B-2502) in 3% radiochemical yield (non-decay-corrected). [^{18}F]2 was obtained in radiochemical purity >98% with a molar activity >37 GBq/μmol, suitable for further evaluation.

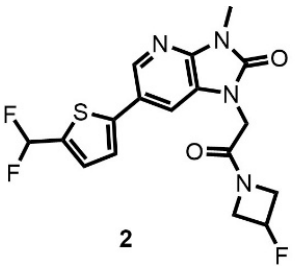
In vitro autoradiography

To investigate the *in vitro* binding properties, autoradiography studies of [^{18}F]2 were performed in rat brain sections. [^{18}F]2 showed high and regionally specific accumu-



Scheme 1. Synthesis of compound 2.

Table 1. Physicochemical and pharmacological properties of compound 2



Parameters	MW[a]	logP[b]	logD[b]	tPSA[b]	MPO score[b]	IC_{50} (nM)[d]
Value	396.39	1.64	1.60 (1.73)[c]	84.99	5.7	10

[a]Calculated with ChemDraw 21. [b]Calculated with ACD Labs. [c]Measured by "shake-flask" method. [d]Adopted from ref. [26].

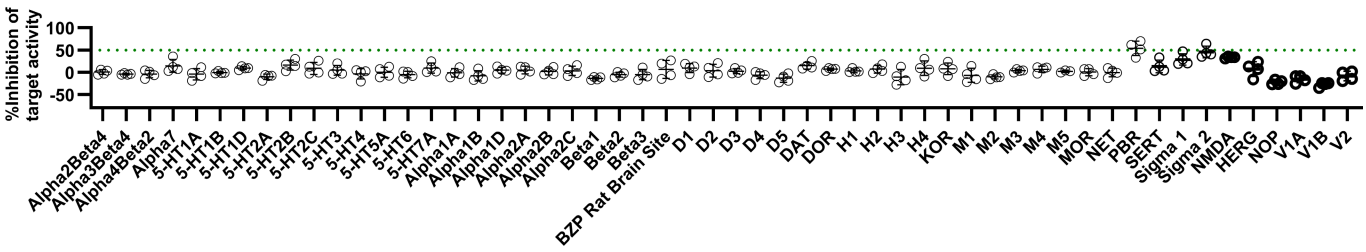
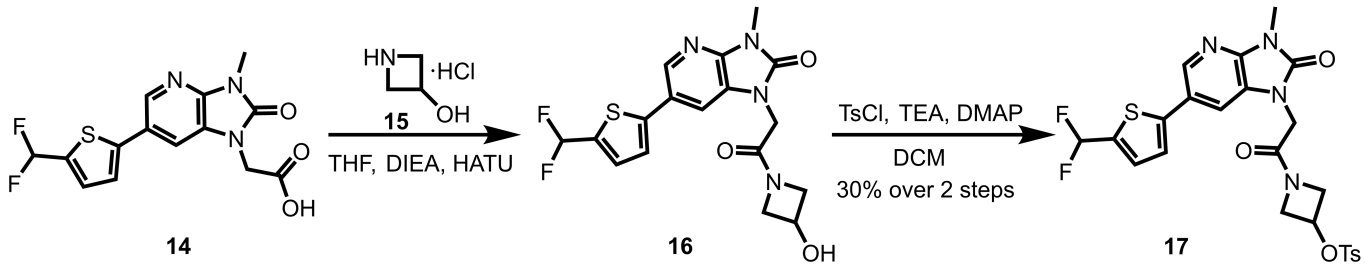
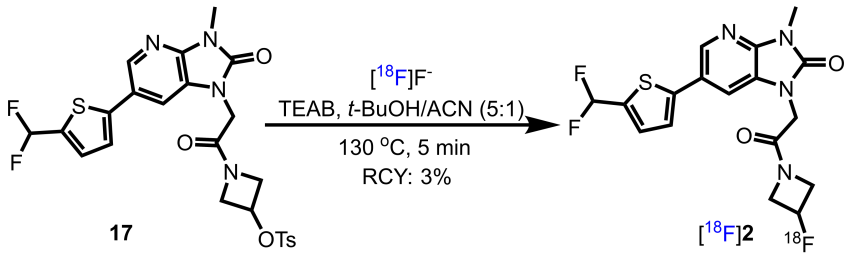


Figure 2. Off-target pharmacological evaluation of compound 2 at a concentration of 10 μM against major CNS targets.



Scheme 2. Synthesis of the labeling precursor 17.



Scheme 3. Radiosynthesis of [^{18}F]2 ([^{18}F]N2B-2502).

lation under baseline conditions (**Figure 3A**). Co-incubation with non-radioactive compound 2 or Ro 25-6981, a GluN2B-targeted NMDA receptor antagonist, eliminated this uptake throughout the section. Quantitative analysis confirmed this pattern (**Figure 3B**). Tracer accumulation was high in cortex, hippocampus, and striatum, and low in cerebellum. This pattern is consistent with the reported regional distribution of GluN2B, which is enriched in the cortex, hippocampus, striatum, relative to cerebellum [2].

PET imaging

We next conducted *in vivo* PET imaging of [^{18}F]2 in mice. Under baseline conditions, [^{18}F]2 showed low brain uptake, with a whole-brain SUV of approximately 0.4 at early time points, followed by gradual washout over 60 min (**Figure 4A**). Baseline time-activity curves for the cortex, hippocampus, and striatum were similar to the whole-brain curve, with no apparent regional differences (**Figure 4C**). Pretreatment with non-radioactive compound 2 or Ro 25-6981 did not reduce brain uptake (**Figure 4B**). This finding provided no evidence of specific binding *in vivo*, in contrast to the region-specific blocking observed by autoradiography (**Figure 3**). The increase in brain SUV after blocking may reflect blocking of GluN2B in peripheral tissues, which would increase the fraction of systemic tracer available for brain delivery. To determine whether [^{18}F]2 is a substrate of P-glycoprotein (P-gp), we performed PET imaging after pretreatment with a P-gp inhibitor (Elacridar, 3 mg/kg). As shown in **Figure 4D**, P-gp inhibition increased whole-brain tracer uptake by over 70% based on area under the curve (AUC) of the time-activity curves (7.1 to 12.4). This result indicates that [^{18}F]2 might be a substrate of P-gp, and future structural modification should aim to reduce susceptibility to P-gp-mediated efflux.

Biodistribution

CD-1 mice underwent *ex vivo* whole-body biodistribution analysis after injection of [^{18}F]2, with tissues harvested at 5, 15, 30, and 60 min to characterize its distribution and clearance profile (**Figure 5**). The small intestine, kidney, and liver accumulated the highest levels of radioactivity at early time points (>5 %ID/g), and this activity cleared progressively over 60 min, a profile consistent with combined hepatobiliary and renal elimination of the tracer. Brain uptake remained low throughout the study (0.9 %ID/g at 5 min), confirming the low brain penetration observed by PET imaging. Bone radioactivity did not increase over the 60 min, indicating that *in vivo* defluorination of [^{18}F]2 was minimal.

Radiometabolite analysis

To assess the *in vivo* metabolic stability of [^{18}F]2, we conducted an *ex vivo* metabolism study in mice at 30 min post-injection. Parent fraction analysis showed that the intact parent tracer accounted for 88.1% of total radioactivity in the brain and 45.9% in plasma (**Figure 6**). The high brain parent fraction indicates that [^{18}F]2 is metabolically stable in brain tissue at this time point. The lower plasma parent fraction indicates more rapid peripheral metabolism and should be considered in future kinetic modeling based on a plasma input function.

Discussion

We synthesized and evaluated [^{18}F]2 ([^{18}F]N2B-2502), a novel imidazo[4,5-*b*]pyridin-2-one radioligand for GluN2B. This chemotype is structurally distinct from the 3-benzazepin-1-ol scaffold that is shared by most GluN2B radioligands reported to date, including (*R*)-[^{11}C]Me-NB1 and its derivatives. Compound 2 has no chiral centers, in contrast to the NB1 series, which requires enantiomer separation and shows enantiomer-dependent GluN2B/σ1 selectivity. The imidazo[4,5-*b*]pyridin-2-one core is capable of binding GluN2B with an IC_{50} in the low nanomolar range. Compound 2 also showed no significant activity at σ1, the receptor responsible for confounding the specific binding of (*R*)-[^{11}C]Me-NB1 *in vivo*. A key finding of this study is a discrepancy between *in vitro* and *in vivo* results. *In vitro* autoradiography showed region-specific binding of [^{18}F]2 to the rat brain, matching reported distribution patterns of GluN2B. The tracer binding was fully blocked by compound 2 and by the commercially available GluN2B ligand, Ro 25-6981. *In vivo* PET imaging showed low brain uptake and no evidence of specific binding under the same blocking conditions. P-gp inhibition increased brain uptake by over 70%, indicating P-gp-mediated efflux at the blood-brain barrier as the main factor for this discrepancy. The PET imaging study was conducted in two animals (n = 2), consistent with its exploratory purpose of determining whether [^{18}F]2 should be advanced as a GluN2B PET radioligand. Neither animal showed evidence of a blocking effect, whereas P-gp inhibition substantially increased brain uptake. These findings suggest that [^{18}F]2 has limited potential for further development. This limitation is distinct from those reported for other GluN2B radioligands. Although the physicochemical profile of compound 2 meets standard criteria for CNS penetration (TPSA below 90 Å^2 and favorable CNS MPO score), the compound is likely a P-gp substrate. This finding shows

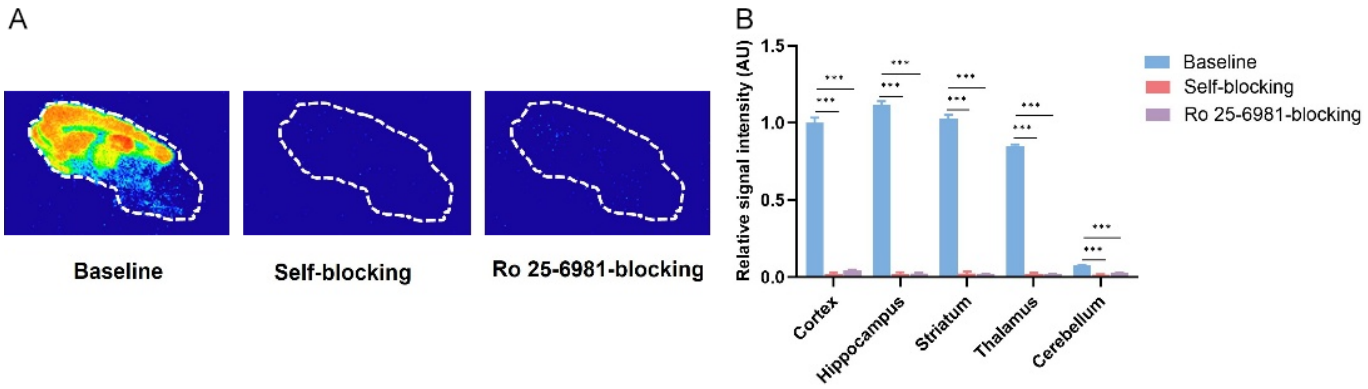


Figure 3. *In vitro* autoradiography of [^{18}F]2 in rat brain sections. A. Autoradiographic images under baseline conditions and after blocking with cold compound 2 (self-blocker, 10 μM) and Ro 25-6981 (10 μM). B. Quantification of relative signal intensity in five brain regions under baseline and blocking conditions. Data are presented as mean ± SD, n = 3. Asterisks indicate significant differences from baseline (***P ≤ 0.001).

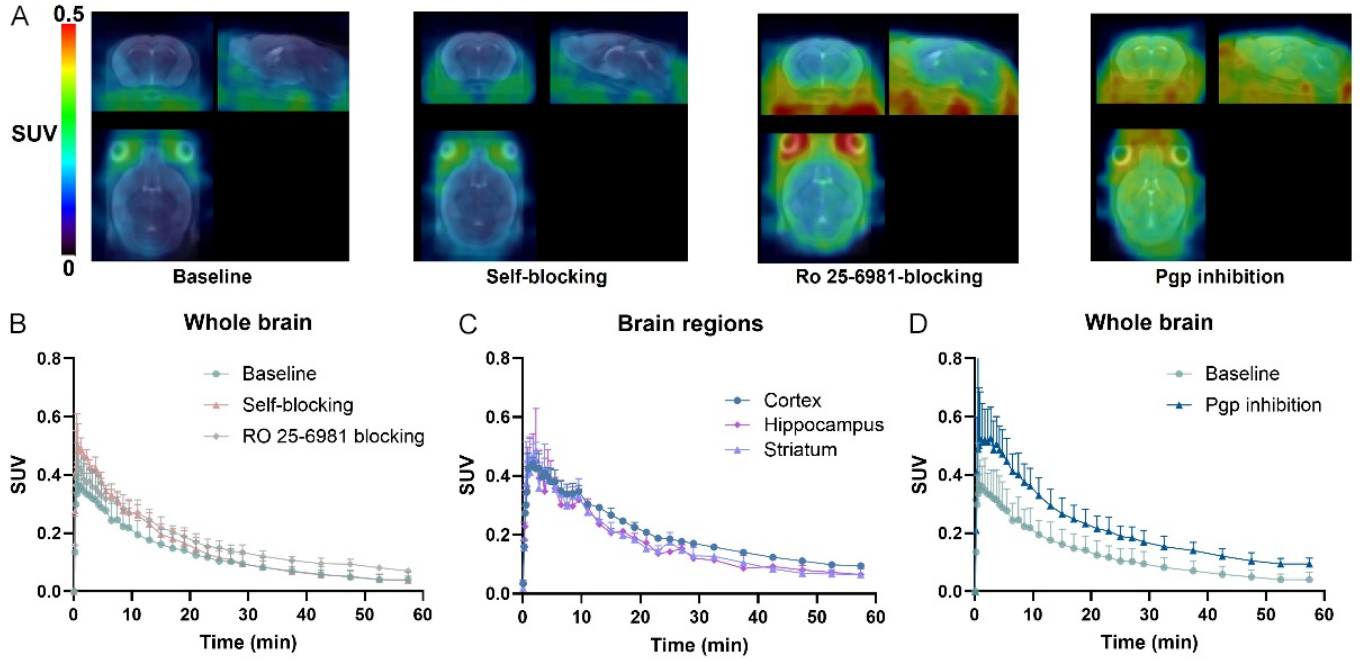


Figure 4. *In vivo* PET imaging of [^{18}F]2 in mice (n = 2). A. Representative PET images (coronal, sagittal, and horizontal planes) under baseline conditions, after blocking with non-radioactive compound 2 (self-blocking) or Ro 25-6981, and after P-glycoprotein (P-gp) inhibition. B. Whole-brain time-activity curves under baseline, self-blocking, and Ro 25-6981-blocking conditions. C. Time–activity curves of selected brain regions under baseline conditions. D. Whole-brain time-activity curves under baseline conditions and after P-gp inhibition.

that *in silico* or *in vitro* physicochemical parameters alone are insufficient to predict P-gp-mediated efflux liability. Species differences between the autoradiography (rat) and *in vivo* (mouse) studies, along with plasma protein binding reducing the free fraction of [^{18}F]2 available for blood-brain barrier penetration, may also contribute to this discrepancy independent of P-gp efflux. We did not pursue further optimization of the radiosynthesis of [^{18}F]2, since the low brain uptake of [^{18}F]2 is likely driven by P-gp-mediated efflux rather than by any limitation in radiochemical yield, and a higher yield would not resolve this issue. Several limitations of this study should be noted. The PET imaging studies were performed in a small number of animals (n = 2), and radiometabolite analysis was limited to a single time point (30 min). These experiments were intended primarily to determine whether [^{18}F]2 warranted further development rather than to provide a full kinetic or metabolic characterization. The radiochemical yield of [^{18}F]2 was also relatively low (3%, non-decay-corrected), although it was sufficient for the studies reported here. Finally, although [^{18}F]2 showed region-specific and blockable binding in autoradiography, no specific binding was observed in vivo. The increased brain uptake following P-gp inhibition suggests that limited brain penetration due to efflux transporter activity contributed to this discrepancy. Therefore, assessment of efflux transporter in-

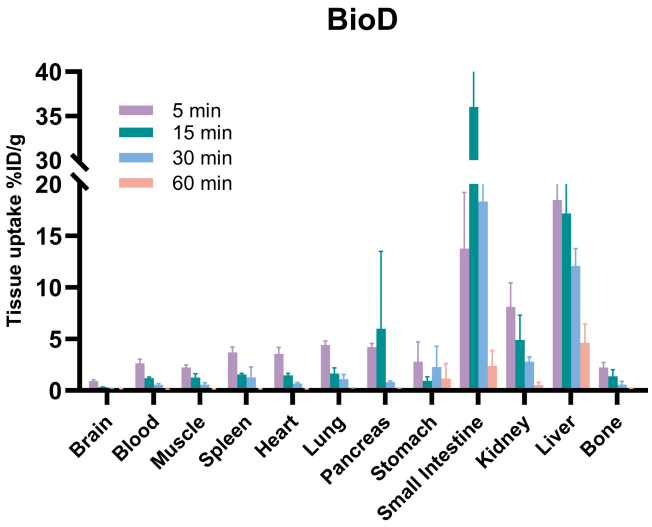


Figure 5. Whole-body *ex vivo* biodistribution studies in mice at four different time points (5, 15, 30, and 60 min) post-injection of [^{18}F]2. Data are expressed as %ID/g (mean ± SD, n = 4). %ID/g = injected dose per gram of wet tissue.

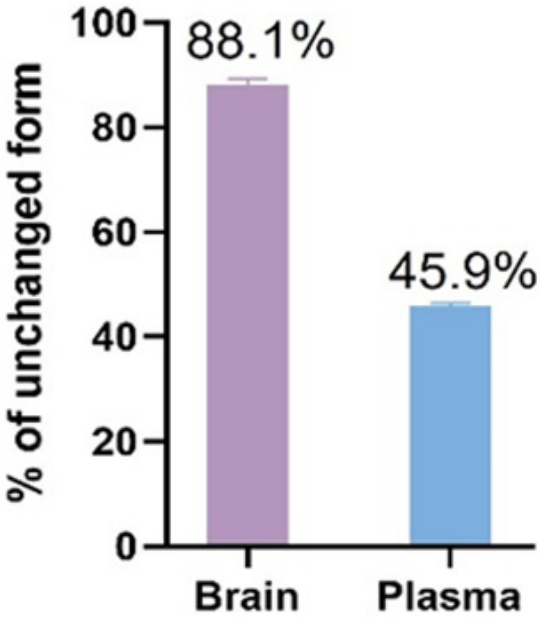


Figure 6. *Ex vivo* metabolite analysis of [^{18}F]2 in mouse brain and plasma at 30 min post-injection. Data are expressed as % of unchanged (intact parent) form. Data are presented as mean ± SD, n = 2.

teractions should be incorporated early in the lead optimization process for this chemotype. Strategies such as reducing topological polar surface area and modifying substituents recognized by the transporter binding pocket may clarify whether the imidazo[4,5-*b*]pyridin-2-one core can be developed into a GluN2B radioligand suitable for quantitative PET imaging.

Conclusion

In summary, we synthesized and evaluated [^{18}F]2 ([^{18}F]N2B-2502), an imidazo[4,5-*b*]pyridin-2-one radioligand for the utility to image GluN2B-containing NMDA receptors. Compound 2 exhibited favorable physicochemical properties and high selectivity against a panel of major CNS targets, including no significant activity at sigma 1. *In vitro* autoradiography demonstrated high, region-specific binding in rat brain, consistent with the reported distribution of GluN2B. *In vivo* PET imaging showed low brain uptake and no evidence of specific binding. P-gp inhibition increased brain uptake by over 70%, indicating that [^{18}F]2 might be a substrate of P-gp. Efflux at the blood-brain barrier limits the brain uptake of [^{18}F]2 and precludes its use as a PET radioligand for GluN2B in its current form. Structural modification to reduce P-gp-mediated efflux may improve the brain penetration of this chemotype.

Materials and methods

General

All chemicals and solvents were purchased from commercially available sources and used without further purification unless otherwise noted. ^{1}H and ^{13}C NMR spectra were recorded on a Bruker spectrometer at 400 MHz for ^{1}H and 100 MHz for ^{13}C. Chemical shifts are reported in ppm relative to TMS. High-performance liquid chromatography (HPLC) was performed using a Shimadzu LC-2010A HT system. HPLC-MS analyses were performed on an Agilent 6120B single-quadrupole mass spectrometer equipped with an electrospray ionization (ESI) source. High-resolution mass spectrometry (HRMS) was performed on a Thermo Fisher Scientific UPLC-ESI-Q-Orbitrap mass spectrometer operated in positive ion mode. Purity of all final compounds was ≥95%, as determined by analytical HPLC. All animal experiments were performed in compliance with institutional ethical guidelines under protocols approved by the Emory University IACUC (protocol numbers PROTO202200003 and PROTO202200076).

Chemistry

Synthesis of 5-bromo-N-methyl-3-nitropyridin-2-amine (4): To a solution of 2,5-dibromo-3-nitropyridine 3 (11 g, 39.02 mmol) in EtOH (100 mL) was added $MeNH_2$ (40% w/w in water, 9.0 g, 115.27 mmol). The final mixture was stirred at 55°C for 2 h. The reaction mixture was filtrated, and the cake was washed with water and dried to give 5-bromo-*N*-methyl-3-nitropyridin-2-amine (4, 9.0 g, 99%) as a yellow solid, used directly for the next step. LC-MS (ESI$^+$): m/z, 233.0 [M+H]$^+$.

Synthesis of 5-bromo-N2-methylpyridine-2,3-diamine (5): To a solution of 5-bromo-N-methyl-3-nitropyridin-2-amine 4 (7.8 g, 33.6 mmol) in EtOH (50 mL) and H_2O (50 mL) was added Fe (9.4 g, 168 mmol) and NH_4Cl (9.2 g, 171 mmol). The final mixture was stirred at 80°C for 2 h. The

reaction mixture was filtrated, and the filtrate was concentrated and purified by flash column chromatography (petroleum ether/ethyl acetate = 1/1) to give 5-bromo-N2-methylpyridine-2,3-diamine (5, 4.4 g, 65%) as a black solid, used directly for the next step.

Synthesis of 6-bromo-3-methyl-1,3-dihydro-2H-imidazo-[4,5-b]pyridin-2-one (6): To a solution of 5-bromo-N2-methylpyridine-2,3-diamine 5 (4.0 g, 0.02 mol) in THF (60 mL) was added CDI (6.45 g, 0.04 mol). The mixture was stirred at 60°C for 2 h. The reaction mixture was filtrated, and the filter cake was collected to give 6-bromo-3-methyl-1,3-dihydro-*2H*-imidazo[4,5-*b*]pyridin-2-one (6, 3.6 g, 79%) as pale green solid, used directly for the next step.

Synthesis of ethyl 2-(6-bromo-3-methyl-2-oxo-2,3-dihydro-1H-imidazo[4,5-b]pyridin-1-yl)acetate (8): To a solution of 6-bromo-3-methyl-1,3-dihydro-*2H*-imidazo[4,5-*b*]pyridin-2-one 6 (300 mg, 1.32 mmol) in MeCN (10 mL) was added ethyl 2-bromoacetate 7 (230 mg, 1.39 mmol) and K_2CO_3 (547 mg, 3.96 mmol). The mixture was stirred at 80°C overnight. The reaction mixture was filtrated, and the filtrate was concentrated and purified by flash column chromatography (petroleum ether/ethyl acetate = 2/1) to give ethyl 2-(6-bromo-3-methyl-2-oxo-2,3-dihydro-*1H*-imidazo[4,5-*b*]pyridin-1-yl)acetate (8, 352 mg, 85%) as a white solid, used directly for the next step.

Synthesis of ethyl 2-(3-methyl-2-oxo-6-(4,4,5,5-tetramethyl-1,3,2-dioxaborolan-2-yl)-2,3-dihydro-1H-imidazo[4,5-b]pyridin-1-yl)acetate (9): To a solution of ethyl 2-(6-bromo-3-methyl-2-oxo-2,3-dihydro-*1H*-imidazo[4,5-*b*]pyridin-1-yl)acetate 8 (400 mg, 1.3 mmol) in dioxane (7 mL) was added B_2Pin_2 (357 mg, 1.4 mmol), KOAc (314 mg, 3.2 mmol) and Pd(dppf)Cl_2 (95 mg, 0.1 mmol) under a nitrogen atmosphere. The mixture was stirred at 80°C for 2 h. The reaction mixture was poured into water and extracted with ethyl acetate. The organic layer was washed with brine, dried over Na_2SO_4 and concentrated to give ethyl 2-(3-methyl-2-oxo-6-(4,4,5,5-tetramethyl-1,3,2-dioxaborolan-2-yl)-2,3-dihydro-*1H*-imidazo[4,5-*b*]pyridin-1-yl) acetate (9, 390 mg, 84%) as a black solid, used directly for the next step.

Synthesis of ethyl 2-(6-(5-(difluoromethyl)thiophen-2-yl)-3-methyl-2-oxo-2,3-dihydro-1H-imidazo[4,5-b]pyridin-1-yl) acetate (11): To a solution of 2-bromo-5-(difluoromethyl) thiophene 10 (200 mg, 0.94 mmol) in dioxane (4 mL) and H_2O (1 mL) was added ethyl 2-(3-methyl-2-oxo-6-(4,4,5,5-tetramethyl-1,3,2-dioxaborolan-2-yl)-2,3-dihydro-*1H*-imidazo[4,5-*b*]pyridin-1-yl)acetate 9 (373 mg, 1.03 mmol), K_3PO_4 (499 mg, 2.35 mmol) and Xphos-Pd-G2 (37 mg, 0.05 mmol). The mixture was stirred at 70°C for 1 h under a nitrogen atmosphere. The reaction mixture was poured into water and extracted with ethyl acetate. The organic layer was washed with brine, dried over Na_2SO_4 and concentrated and purified by flash column chromatography (petroleum ether/ethyl acetate = 1/1) to give ethyl 2-(6-(5-(difluoromethyl)thiophen-2-yl)-3-methyl-2-oxo-2,3-dihydro-*1H*-imidazo[4,5-*b*]pyridin-1-yl)acetate (11, 150 mg, 43%) as a white solid, used directly for the next step.

Synthesis of 2-(6-(5-(difluoromethyl)thiophen-2-yl)-3-methyl-2-oxo-2,3-dihydro-1H-imidazo[4,5-b]pyridin-1-yl)acetic acid (12): To a solution of ethyl 2-(6-(5-(difluoromethyl) thiophen-2-yl)-3-methyl-2-oxo-2,3-dihydro-*1H*-imidazo[4,5-*b*]pyridin-1-yl)acetate 11 (130 mg, 0.35 mmol) in THF (3 mL) and H_2O (1 mL) was added LiOH (21 mg, 0.89 mmol). The mixture was stirred at room temperature overnight. The reaction mixture was poured into water and extracted with ethyl acetate. The organic layer was washed with brine, dried over Na_2SO_4, and concentrated to give 2-(6-(5-(difluoromethyl)thiophen-2-yl)-3-methyl-2-oxo-2,3-dihydro-*1H*-imidazo[4,5-*b*]pyridin-1-yl)acetic acid (12, 145 mg, crude) as a yellow solid, used directly for the next step without further purification.

Synthesis of 6-(5-(difluoromethyl)thiophen-2-yl)-1-(2-(3-fluoroazetidin-1-yl)-2-oxoethyl)-3-methyl-1,3-dihydro-2H-imidazo[4,5-b]pyridin-2-one (2): To a solution of 2-(6-(5-(difluoromethyl)thiophen-2-yl)-3-methyl-2-oxo-2,3-dihydro-*1H*-imidazo[4,5-*b*]pyridin-1-yl)acetic acid 12 (40 mg, 0.12 mmol) in THF (2 mL) was added 3-fluoroazetidine 13 (14 mg, 0.13 mmol), HATU (91 mg, 0.24 mmol) and DIEA (47 mg, 0.36 mmol). The mixture was stirred at room temperature for 1 h. The reaction mixture was poured into water and extracted with ethyl acetate. The organic layer was washed with brine, dried over Na_2SO_4, concentrated and purified by preparative HPLC to give 6-(5-(difluoromethyl)thiophen-2-yl)-1-(2-(3-fluoroazetidin-1-yl)-2-oxoethyl)-3-methyl-1,3-dihydro-*2H*-imidazo[4,5-*b*] pyridin-2-one (2, 12 mg, 26% over 2 steps) as a white solid. ^{1}H NMR (400 MHz, Chloroform-*d*) δ 8.34 (d, *J* = 1.8 Hz, 1H), 7.46 (d, *J* = 1.9 Hz, 1H), 7.27 (d, *J* = 3.2 Hz, 1H), 7.22-7.15 (m, 1H), 6.84 (t, *J* = 56.0 Hz, 1H), 5.37 (dtt, *J* = 56.1, 6.3, 3.4 Hz, 1H), 4.73-4.53 (m, 2H), 4.51 (s, 1H), 4.42 (t, *J* = 10.4 Hz, 1H), 4.39-4.28 (m, 1H), 4.19 (dd, *J* = 23.9, 11.9 Hz, 1H), 3.54 (s, 3H). ^{13}C NMR (100 MHz, Chloroform-*d*) δ 166.08 (s), 153.71 (s), 143.80 (s), 143.53 (s), 138.55 (s), 135.72 (s), 128.60 (t, *J* = 6.9 Hz), 124.37 (d, *J* = 16.1 Hz), 123.40 (s), 113.78 (s), 112.93 (s), 111.43 (s), 81.64 (d, *J* = 206.7 Hz), 57.41 (dd, *J* = 159.8, 26.5 Hz), 41.10 (s), 26.52 (s). LCMS (ESI$^+$): m/z, 397.0 [M+H]$^+$. HRMS (ESI): exact mass calcd for $C_{17}H_{16}F_3N_4O_2S^+$ [M+H$^+$], 397.0941; found, 397.0939.

Synthesis of 6-(5-(difluoromethyl)thiophen-2-yl)-1-(2-(3-hydroxyazetidin-1-yl)-2-oxoethyl)-3-methyl-1,3-dihydro-2H-imidazo[4,5-b]pyridin-2-one (16): To a solution of 2-(6-(5-(difluoromethyl)thiophen-2-yl)-3-methyl-2-oxo-2,3-dihydro-*1H*-imidazo[4,5-*b*]pyridin-1-yl)acetic acid 14 (250 mg, 0.74 mmol) in THF (8 mL) was added azetidin-3-ol hydrochloride 15 (88 mg, 0.81 mmol), HATU (563 mg, 1.48 mmol) and DIEA (287 mg, 2.22 mmol). The mixture was stirred at room temperature for 1 h. The reaction mixture was poured into water and extracted with ethyl acetate. The organic layer was washed with brine, dried over Na_2SO_4 and concentrated to give 6-(5-(difluoromethyl)

thiophen-2-yl)-1-(2-(3-hydroxyazetidin-1-yl)-2-oxoethyl)-3-methyl-1,3-dihydro-2H-imidazo[4,5-*b*]pyridin-2-one (16, 450 mg, crude) as a white solid, used directly for the next step without further purification.

Synthesis of 1-(2-(6-(5-(difluoromethyl)thiophen-2-yl)-3-methyl-2-oxo-2,3-dihydro-1H-imidazo[4,5-b]pyridin-1-yl) acetyl)azetidin-3-yl 4-methylbenzenesulfonate (17): To a solution of 6-(5-(difluoromethyl)thiophen-2-yl)-1-(2-(3-hydroxyazetidin-1-yl)-2-oxoethyl)-3-methyl-1,3-dihydro-*2H*-imidazo[4,5-*b*]pyridin-2-one 16 (300 mg, 0.76 mmol) in DCM (6 mL) was added TsCl (217 mg, 1.14 mmol), TEA (154 mg, 1.52 mmol) and DMAP (9.3 mg, 0.08 mmol). The mixture was stirred at room temperature overnight. The reaction mixture was poured into water and extracted with ethyl acetate. The organic layer was washed with brine, dried over Na_2SO_4, concentrated and purified by flash column chromatography (ethyl acetate) to give 1-(2-(6-(5-(difluoromethyl)thiophen-2-yl)-3-methyl-2-oxo-2,3-dihydro-*1H*-imidazo[4,5-*b*]pyridin-1-yl)acetyl)azetidin-3-yl 4-methylbenzenesulfonate (17, 82.17 mg, 30% over 2 steps) as a white solid. ^{1}H NMR (400 MHz, Chloroform-d) δ 8.37 (d, J = 1.9 Hz, 1H), 7.91-7.80 (m, 2H), 7.78 (d, J = 1.9 Hz, 1H), 7.56-7.47 (m, 4H), 7.27 (d, J = 55.2 Hz, 1H), 5.22 (tt, J = 6.9, 3.9 Hz, 1H), 4.62 (d, J = 1.7 Hz, 2H), 4.61-4.52 (m, 1H), 4.36-4.24 (m, 1H), 4.17 (dd, J = 11.0, 6.6 Hz, 1H), 3.81 (dd, J = 11.3, 3.9 Hz, 1H), 3.36 (s, 3H), 2.44 (s, 3H). ^{13}C NMR (100 MHz, DMSO-d_6) δ 166.53 (s), 153.93 (s), 146.18 (s), 144.37 (s), 143.97 (s), 138.03 (s), 134.79 (t, J = 25.4 Hz), 132.57 (s), 130.91 (s), 130.75 (s), 128.23 (s), 124.97 (s), 124.03 (s), 123.52 (s), 114.73 (s), 112.45 (s), 110.10 (s), 69.29 (s), 57.07 (s), 55.66 (s), 26.34 (s), 21.63 (s). LCMS (ESI$^+$): m/z, 549.0 [M+H]$^+$. HRMS (ESI): exact mass calcd for $C_{24}H_{23}F_2N_4O_5S_2^+$ [M+H$^+$], 549.1072; found, 549.1077.

Radiochemistry

[^{18}F]Fluoride was generated by proton irradiation of >98% enriched [^{18}O]H_2O *via* the ^{18}O(p,n)^{18}F reaction, using an 18 MeV beam on a GE PETrace 880 cyclotron (GE Healthcare). Radiosynthesis was carried out either manually or *via* an automated Trasis AllInOne™ synthesizer (both methods gave comparable results). Target water containing [^{18}F]Fluoride (~1 GBq) was passed through a Sep-Pak QMA Plus Light cartridge to capture the activity, which was then recovered by passing a solution of Et_4NHCO_3 (TEAB, 2 mg) in MeOH (1.0 mL) through the cartridge in the direction opposite to loading. Residual water was removed by three cycles of azeotropic drying with anhydrous MeCN at 110°C under a nitrogen stream. A solution of precursor 17 (2 mg) in dry *t*-BuOH/MeCN (420 µL, 5:1) was then added, and the reaction mixture was heated at 130°C for 5 min. Following dilution with HPLC mobile phase, the crude reaction mixture was purified by semi-preparative HPLC on a Phenomenex Luna C18(2) column (5 µm, 10 × 250 mm), eluting with MeCN/0.1% TEA aqueous solution (32/68, v/v) at a flow rate of 5.0 mL/min. The identity, radiochemical purity, and molar activity of [^{18}F]2 were confirmed by analytical radio-HPLC on an Agilent 1100 series system equipped with a Phenomenex Luna C-18 column (5 µm, 4.6 × 150 mm), a UV detector (254 nm), and a LabLogic in-line radioactivity detector. The mobile phase consisted of MeCN and 0.1% TEA aqueous solution (40/60, v/v) at a flow rate of 1.0 mL/min.

In vitro autoradiography

Cryosectioned Sprague-Dawley rat brain tissue (14 µm) was embedded in Tissue-Tek® O.C.T. and stored at -80°C prior to use. Sections were equilibrated for 10 min at room temperature in 50 mM Tris buffer containing 0.1% BSA (200 mL), then incubated with [^{18}F]2 (1 µCi/mL) in the same buffer for 30 min. Blocking sections received the same incubation in the presence of 10 µM non-radioactive compound 2 or Ro 25-6981. Sections were subsequently rinsed once in the Tris/BSA buffer (5 min), twice in Tris buffer without BSA (2 min each), and twice in distilled water (5 s each), then air-dried. Dried sections were exposed to a phosphor imaging plate (BAS-MS2025, GE Healthcare) for 12 h and imaged on an Amersham Typhoon system (Cytiva, USA).

PET imaging

Anesthetized CD-1 mice underwent PET imaging on a Molecubes β-CUBE PET scanner (Bruker, Belgium). Dynamic images were acquired over 60 min following tail-vein injection of [^{18}F]2 (~80 µCi). Images were reconstructed and analyzed using PMOD software (v4.3; PMOD Technologies, Switzerland). Blocking studies involved intravenous administration of non-radioactive compound 2 or Ro 25-6981 (3 mg/kg) 10 min prior to tracer injection. To assess P-gp-mediated efflux, elacridar (3 mg/kg) was injected intravenously by the same pre-injection schedule.

Whole-body biodistribution

CD-1 mice (n = 4 per time point) were administered [^{18}F]2 (~20 µCi, 0.1 mL) by tail-vein injection and were euthanized by cervical dislocation at 5, 15, 30, or 60 min post-injection. Brain, blood, muscle, spleen, heart, lung, pancreas, stomach, small intestine, kidney, liver, and bone were harvested and weighed, and tissue radioactivity was measured on a Wizard automatic gamma counter (PerkinElmer, USA). Radioactivity was decay-corrected to the time of injection and expressed as percent injected dose per gram of tissue (%ID/g).

Radiometabolite analysis

CD-1 mice (n = 2) were administered [^{18}F]2 (~400 µCi, 0.1 mL) by intravenous injection and were euthanized by decapitation at 30 min post-injection. Brain tissue and plasma were collected immediately, homogenized in acetonitrile, and centrifuged to remove precipitated protein. The supernatant was analyzed by semi-preparative

HPLC to collect the fractions every 0.5 min. Radioactivity in each fraction was measured on a Wizard automatic gamma counter (PerkinElmer, USA), and the parent fraction was calculated as the percentage of total radioactivity co-eluting with authentic [^{18}F]2. Data were plotted using GraphPad Prism.

Acknowledgements

We thank Emory Center for Systems Imaging Radiopharmacy (Ronald J. Crowe, RPh, BCNP; Karen Dolph, RPh; M. Shane Waldrep) & Department of Radiology and Imaging Sciences, Emory University School of Medicine for general support. We gratefully acknowledge Trasis (Ans, Belgium) for technical support with radiosynthesis automation. We also thank the National Institute of Mental Health's Psychoactive Drug Screening Program (NIMH PDSP) for compound off-target screening. S.H.L. gratefully acknowledges the support provided, in part, by the NIH grants (AG083084, AG075444, AG066511, S10OD034326), Emory Radiology Chair Fund, and Emory School of Medicine Endowed Directorship.

Disclosure of conflict of interest

None.

Address correspondence to: Yinlong Li and Steven H. Liang, Department of Radiology and Imaging Sciences, Emory University, 1364 Clifton Road, Atlanta, Georgia 30322, The United States. E-mail: yinlong.li@emory.edu (YLL); steven.liang@emory.edu (SHL)

References

[1] Traynelis SF, Wollmuth LP, McBain CJ, Menniti FS, Vance KM, Ogden KK, Hansen KB, Yuan H, Myers SJ and Dingledine R. Glutamate receptor ion channels: structure, regulation, and function. Pharmacol Rev 2010; 62: 405-496.

[2] Paoletti P, Bellone C and Zhou Q. NMDA receptor subunit diversity: impact on receptor properties, synaptic plasticity and disease. Nat Rev Neurosci 2013; 14: 383-400.

[3] Bliss TV and Collingridge GL. A synaptic model of memory: long-term potentiation in the hippocampus. Nature 1993; 361: 31-39.

[4] Wenzel A, Fritschy JM, Mohler H and Benke D. NMDA receptor heterogeneity during postnatal development of the rat brain: differential expression of the NR2A, NR2B, and NR2C subunit proteins. J Neurochem 1997; 68: 469-478.

[5] Jin DH, Jung YW, Ko BH and Moon IIS. Immunoblot analyses on the differential distribution of NR2A and NR2B subunits in the adult rat brain. Mol Cells 1997; 7: 749-754.

[6] Endele S, Rosenberger G, Geider K, Popp B, Tamer C, Stefanova I, Milh M, Kortüm F, Fritsch A, Pientka FK, Hellenbroich Y, Kalscheuer VM, Kohlhase J, Moog U, Rappold G, Rauch A, Ropers HH, von Spiczak S, Tönnies H, Villeneuve N, Villard L, Zabel B, Zenker M, Laube B, Reis A, Wieczorek D, Van Maldergem L and Kutsche K. Mutations in GRIN2A and GRIN2B encoding regulatory subunits of NMDA receptors cause variable neurodevelopmental phenotypes. Nat Genet 2010; 42: 1021-1026.

[7] Hu NW, Klyubin I, Anwyl R and Rowan MJ. GluN2B subunit-containing NMDA receptor antagonists prevent Aβ-mediated synaptic plasticity disruption in vivo. Proc Natl Acad Sci U S A 2009; 106: 20504-20509.

[8] Steece-Collier K, Chambers LK, Jaw-Tsai SS, Menniti FS and Greenamyre JT. Antiparkinsonian actions of CP-101,606, an antagonist of NR2B subunit-containing n-methyl-d-aspartate receptors. Exp Neurol 2000; 163: 239-243.

[9] Mony L, Kew JN, Gunthorpe MJ and Paoletti P. Allosteric modulators of NR2B-containing NMDA receptors: molecular mechanisms and therapeutic potential. Br J Pharmacol 2009; 157: 1301-1317.

[10] Rong J, Haider A, Jeppesen TE, Josephson L and Liang SH. Radiochemistry for positron emission tomography. Nat Commun 2023; 14: 3257.

[11] Deng X, Rong J, Wang L, Vasdev N, Zhang L, Josephson L and Liang S. Chemistry for positron emission tomography: recent advances in ^{11}C-, ^{18}F-, ^{13}N-, and ^{15}O-labeling reactions. Angew Chem Int Ed Engl 2019; 58: 2580-2605.

[12] Haradahira T, Maeda J, Okauchi T, Zhang MR, Hojo J, Kida T, Arai T, Yamamoto F, Sasaki S, Maeda M, Suzuki K and Suhara T. Synthesis, in vitro and in vivo pharmacology of a C-11 labeled analog of CP-101,606, (±)threo-1-(4-hydroxyphenyl)-2-[4-hydroxy-4-(p-[11C]methoxyphenyl) piperidino]-1-propanol, as a PET tracer for NR2B subunit-containing NMDA receptors. Nucl Med Biol 2002; 29: 517-525.

[13] van der Aart J, Yaqub M, Kooijman EJM, Bakker J, Langermans JAM, Schuit RC, Hofman MBM, Christiaans JAM, Lammertsma AA, Windhorst AD and van Berckel BNM. Evaluation of the novel PET tracer [^{11}C]HACH242 for imaging the GluN2B NMDA receptor in non-human primates. Mol Imaging Biol 2019; 21: 676-685.

[14] Krämer SD, Betzel T, Mu L, Haider A, Herde AM, Boninsegni AK, Keller C, Szermerski M, Schibli R, Wünsch B and Ametamey SM. Evaluation of ^{11}C-Me-NB1 as a potential PET radioligand for measuring GluN2B-containing NMDA receptors, drug occupancy, and receptor cross talk. J Nucl Med 2018; 59: 698-703.

[15] Rischka L, Vraka C, Pichler V, Rasul S, Nics L, Gryglewski G, Handschuh P, Murgaš M, Godbersen GM, Silberbauer LR, Unterholzner J, Wotawa C, Haider A, Ahmed H, Schibli R, Mindt T, Mitterhauser M, Wadsak W, Hahn A, Lanzenberger R, Hacker M and Ametamey SM. First-in-humans brain PET imaging of the GluN2B-containing *N*-methyl-d-aspartate receptor with (R)-^{11}C-Me-NB1. J Nucl Med 2022; 63: 936-941.

[16] Haider A, Herde AM, Krämer SD, Varisco J, Keller C, Frauenknecht K, Auberson YP, Temme L, Robaa D, Sippl W, Schibli R, Wünsch B, Mu L and Ametamey SM. Preclinical evaluation of benzazepine-based PET radioligands (R)- and (S)-^{11}C-Me-NB1 reveals distinct enantiomeric binding patterns and a tightrope walk between GluN2B- and σ1-receptor-targeted PET imaging. J Nucl Med 2019; 60: 1167-1173.

[17] Haider A, Iten I, Ahmed H, Müller Herder A, Gruber S, Krämer SD, Keller C, Schibli R, Wünsch B, Mu L and Ametamey SM. Identification and preclinical evaluation of a radiofluorinated benzazepine derivative for imaging the GluN2B subunit of the ionotropic NMDA receptor. J Nucl Med 2018; 60: 259-66.

[18] Zheng M, Ahmed H, Smart K, Xu Y, Holden D, Kapinos M, Felchner Z, Haider A, Tamagnan G, Carson RE, Huang Y

and Ametamey SM. Characterization in nonhuman primates of (R)-[18F]OF-Me-NB1 and (S)-[18F]OF-Me-NB1 for imaging the GluN2B subunits of the NMDA receptor. Eur J Nucl Med Mol Imaging 2022; 49: 2153-2162.

[19] Ahmed H, Wallimann R, Haider A, Hosseini V, Gruber S, Robledo M, Nguyen TAN, Herde AM, Iten I, Keller C, Vogel V, Schibli R, Wünsch B, Mu L and Ametamey SM. Preclinical development of ^{18}F-OF-NB1 for imaging GluN2B-containing N-methyl-d-aspartate receptors and its utility as a biomarker for amyotrophic lateral sclerosis. J Nucl Med 2021; 62: 259-265.

[20] Ahmed H, Zheng MQ, Smart K, Fang H, Zhang L, Emery PR, Gao H, Ropchan J, Haider A, Tamagnan G, Carson RE, Ametamey SM and Huang Y. Evaluation of (*rac*)-, (*R*)-, and (S)-^{18}F-OF-NB1 for imaging GluN2B subunit-containing N-methyl-d-aspartate receptors in nonhuman primates. J Nucl Med 2022; 63: 1912-1918.

[21] Korff M, Chaudhary A, Li Y, Zhou X, Zhao C, Rong J, Chen J, Xiao Z, Elghazawy NH, Sippl W, Davenport AT, Daunais JB, Wang L, Abate C, Ahmed H, Crowe R, Schmidt TJ, Liang SH, Ametamey SM, Wünsch B and Haider A. Synthesis and biological evaluation of enantiomerically pure (R)- and (S)-[^{18}F]OF-NB1 for imaging the GluN2B subunit-containing NMDA receptors. J Med Chem 2023; 66: 16018-16031.

[22] Cai L, Liow JS, Morse CL, Telu S, Davies R, Frankland MP, Zoghbi SS, Cheng K, Hall MD, Innis RB and Pike VW. Evaluation of ^{11}C-NR2B-SMe and its enantiomers as PET radioligands for imaging the NR2B subunit within the NMDA receptor complex in rats. J Nucl Med 2020; 61: 1212-1220.

[23] Jakobsson JE, Gourni E, Khanapur S, Brito B and Riss PJ. Synthesis and characterization in rodent brain of the subtype-selective NR2B NMDA receptor ligand [^{11}C]Ro04-5595 as a potential radiotracer for positron emission tomography. ACS Omega 2019; 4: 9925-9931.

[24] Sun JY, Kumata K, Chen Z, Zhang YD, Chen JH, Hatori A, Fu HL, Rong J, Deng XY, Yamasaki T, Xie L, Hu K, Fujinaga M, Yu QZ, Shao T, Collier TL, Josephson L, Shao YH, Du YF, Wang L, Xu H, Zhang MR and Liang SH. Synthesis and preliminary evaluation of novel ^{11}C-labeled GluN2B-selective NMDA receptor negative allosteric modulators. Acta Pharmacol Sin 2021; 42: 491-498.

[25] Fu H, Tang W, Chen Z, Belov VV, Zhang G, Shao T, Zhang X, Yu Q, Rong J, Deng X, Han W, Myers SJ, Giffenig P, Wang L, Josephson L, Shao Y, Davenport AT, Daunais JB, Papisov M, Yuan H, Li Z, Traynelis SF and Liang SH. Synthesis and preliminary evaluations of a triazole-cored antagonist as a PET imaging probe ([^{18}F]N2B-0518) for GluN2B subunit in the brain. ACS Chem Neurosci 2019; 10: 2263-2275.

[26] Chrovian CC, Letavic MA, Rech JC, Rudolph DA, Johnson AS, Stenne BM and Wall JL. Substituted 1H-imidazo[4,5-b] pyridin-2(3H)-ones and their use as GluN2B receptor modulators. Janssen Pharmaceutica NV, WO2018/067786A1 2018.